QUANTUM PHYSICS

A photonic platform for donor spin qubits in silicon

Kevin J. Morse,[1] Rohan J. S. Abraham,[1] Adam DeAbreu,[1] Camille Bowness,[1] Timothy S. Richards,[1] Helge Riemann,[2] Nikolay V. Abrosimov,[2] Peter Becker,[3] Hans-Joachim Pohl,[4] Michael L. W. Thewalt,[1] Stephanie Simmons[1]*

Donor spins in silicon are highly competitive qubits for upcoming quantum technologies, offering complementary metal-oxide semiconductor compatibility, coherence (T_2) times of minutes to hours, and simultaneous initialization, manipulation, and readout fidelities near ~99.9%. This allows for many quantum error correction protocols, which will be essential for scale-up. However, a proven method of reliably coupling spatially separated donor qubits has yet to be identified. We present a scalable silicon-based platform using the unique optical properties of "deep" chalcogen donors. For the prototypical $^{77}Se^+$ donor, we measure lower bounds on the transition dipole moment and excited-state lifetime, enabling access to the strong coupling limit of cavity quantum electrodynamics using known silicon photonic resonator technology and integrated silicon photonics. We also report relatively strong photon emission from this same transition. These results unlock clear pathways for silicon-based quantum computing, spin-to-photon conversion, photonic memories, integrated single-photon sources, and all-optical switches.

INTRODUCTION

Scaling up donor spin qubit systems

It has been known for some time that the remarkable coherence (*1*, *2*) and control characteristics (*3*, *4*) of donor spin qubits in silicon, combined with potential complementary metal-oxide semiconductor (CMOS) compatibility, make silicon a highly attractive platform for quantum technologies. However, a scalable coupling strategy robust to manufacturing imperfections has yet to emerge. Early silicon donor-based proposals, such as the Kane proposal (*5*), envisaged large exchange interactions to couple donor spin qubits. These proposals have spurred the development of techniques that now offer near-perfect donor placement (*6*). Nevertheless, the multivalley nature of the silicon conduction band makes exchange coupling vary by up to an order of magnitude if the donor spacing is incorrect by even a single atom (*7*).

A robust spin-photon interface could solve this problem by allowing coupling and readout of qubits using cavity quantum electrodynamics (QED). Unfortunately, the weak magnetic dipole moment of the spins makes a direct magnetic coupling approach using microwave photons and superconducting cavities unsuitable (*8*). A more recent proposal (*9*) involves precisely placing a donor near a Si/SiO_2 interface in the very large electric field regime, where the donor electron is partially ionized and has a ground-state electric dipole moment; the decoherence characteristics of such an environment are presently unknown.

Here, we present a new, scalable platform for donor qubits in silicon that is robust to placement variations and does not modify the spins' isolated ground states, which are responsible for their ultralong coherence times. In short, we propose that the optical and spin properties of chalcogen donors make them uniquely suited for cavity QED–based qubit measurement and coupling using silicon photonic circuits.

The most well-studied silicon donor qubits, namely, the group V hydrogenic "shallow" donors such as phosphorus, do not offer suitable optical transitions. Shallow donors have small binding energies (~45 meV) with excited-state optical transitions in the technically onerous ~3 to 10 THz range and excited-state lifetimes strongly dominated by phonon-assisted relaxation (*10*). Alternatively, shallow donors offer spin-selective near-infrared (NIR), no-phonon, donor-bound exciton transitions (*11*), yet because of the indirect bandgap of silicon, these are very weak optical transitions with highly nonradiative decay (*12*). Despite these limitations, proposals for optically controlling shallow donors have been made (*13*, *14*).

Here, we propose to exploit the electric dipole–allowed optical transitions available to "deep" donors, such as the chalcogen double donors sulfur, selenium, and tellurium (*15*). In their neutral state, these helium-like double donors bind two electrons, with large binding energies (~300 meV). When singly ionized, the remaining electron has an even larger binding energy [614 meV for S^+, 593 meV for Se^+, and 411 meV for Te^+ (*16*)] and a hydrogenic-like (or He^+) orbital structure with optical transitions in the midinfrared (mid-IR). In $^{28}Si:^{77}Se^+$, the optical transitions between the 1s:*A* ground state and the lowest excited state are sufficiently narrow to be electron and nuclear spin selective even at very low, or zero, magnetic field (*15*). These donors can be implanted into the large electric field antinode of photonic structures, far from interface noise sources, and the resulting strong coupling will enable single-spin, single-shot readout at 4.2 K and indirect multi-qubit coupling.

This paper is organized as follows. First, we introduce the system: the qubits and optical transitions under consideration. Next, we present verification data to justify some of the main claims of the proposal. We follow this with the strategy, including candidate readout and multi-qubit coupling schemes, and then conclude by pointing out some additional applications of this approach.

The system

When a single electron is bound to the singly ionized donor $^{77}Se^+$ at low temperatures, the 1s:*A* ground-state spin qubit Hamiltonian is given by

$$H = \frac{g_e \mu_B}{h} B_0 S_z - \frac{g_n \mu_N}{h} B_0 I_z + A\vec{S}\cdot\vec{I}$$

where g_e and g_n are the electron and nuclear *g*-factors, respectively, μ_B and μ_N are the Bohr and nuclear magnetons, respectively, h is Planck's constant, A is the hyperfine constant, and $\vec{S}$ and $\vec{I}$ are the spin

[1]Department of Physics, Simon Fraser University, Burnaby, British Columbia V5A 1S6, Canada. [2]Leibniz-Institut für Kristallzüchtung, 12489 Berlin, Germany. [3]Physikalisch-Technische Bundesanstalt (PTB) Braunschweig, 38116 Braunschweig, Germany. [4]VITCON Projectconsult GmbH, 07745 Jena, Germany.
*Corresponding author. Email: s.simmons@sfu.ca

operators of the electron and nucleus, respectively. Some chalcogen nuclear isotopes have a nonzero spin, in particular ^{33}S (spin $^3/_2$), ^{77}Se (spin $^1/_2$), and ^{123}Te and ^{125}Te (both, spin $^1/_2$). These donors' ground states have the same spin Hamiltonian as the group V donors but with larger hyperfine constants (A) of 312 MHz (1.29 μeV), 1.66 GHz (6.87 μeV), 2.90 GHz (12.0 μeV), and 3.49 GHz (14.4 μeV), respectively (*17*). At zero magnetic field, the hyperfine interaction splits the $^{77}Se^+$ ground-state spin levels into electron-nuclear spin singlet and triplet states.

Perturbation coupling terms, such as those arising due to electric fields (*18*, *19*), strain (*20*), and phonons (*21*), are weak, which in similar (that is, group V) systems result in donor spin qubits' ultralong coherence times in enriched ^{28}Si (*1*). These coherence times rely on the removal of magnetic noise due to the naturally occurring ^{29}Si spin-$^1/_2$ isotope in the host lattice (*22*), which also removes local mass variations that inhomogeneously broaden donors' optical transitions (*23*).

Of the many optical transitions available to chalcogen donors (*15*), excitation to the lowest excited state, 1s:T_2:Γ_7, has the most compelling properties. The sixfold valley degeneracy of silicon gives six sublevels to the "1s" hydrogenic manifold of ^{28}Si:$^{77}Se^+$. Ignoring spin interactions, these levels are split by valley-orbit terms and, in increasing energy, are labeled 1s:A (one level), 1s:T_2 (three levels), and 1s:E (two levels) (Fig. 1A). With spin and associated spin-valley interactions, 12 electronic states exist, and the 6 spin-valley states of 1s:T_2 split into 1s:T_2:Γ_7 (two states) and 1s:T_2:Γ_8 (four states) (hereafter referred to as 1s:Γ_7 and 1s:Γ_8), as seen in Fig. 1B.

Optical coupling between 1s:A and 1s:Γ_7 is forbidden according to effective mass theory (EMT). Here, these transitions are allowed, first, because the 1s:A state is much deeper than the effective mass binding energy and hence is not well approximated by EMT, and second, because of the parity of the valley states involved. 1s:A is a symmetric combination of all six valleys, making it s-like in valley character, whereas all 1s:T_2 states are odd combinations of opposing valleys, making them p-like in valley character. Correspondingly, there exists a large hyperfine interaction in the 1s:A manifold yet a small or negligible hyperfine interaction in the 1s:Γ_7 manifold. The 1s:Γ_7 hybrid spin-valley states in a nonzero magnetic field are represented visually in Fig. 1C and explicitly given by Castner (*24*).

Verification data

To exploit these electric dipole–allowed transitions in the context of a 4 K compatible cavity QED architecture, we perform ensemble characterization and confirm aspects of both the optical and spin degrees of freedom. Here, we show that (i) these target optical transitions emit photons and offer reasonable transition matrix dipole moments to support strong coupling and (ii) these spin qubits are comparable if not superior to ^{31}P donor spin qubits at the target temperatures and magnetic fields.

Our 2 mm × 2 mm × 10 mm ^{28}Si:$^{77}Se^+$–compensated n-type sample [75 parts per million (ppm) ^{29}Si, ~5 × 10^{13} cm^{-3} boron, and 2 × 10^{13} cm^{-3} $^{77}Se^+$ introduced using thermal diffusion; see Materials and Methods] shows that the 1s:A ⇔ 1s:Γ_7 optical transitions have a purely Lorentzian linewidth of 0.87 μeV (*15*) when collected at maximum instrumental resolution (Fig. 1D). We further observe that these 427.3 meV (2902 nm) transitions emit photons when pumped with a 1081 nm near-bandgap light (Fig. 1D), disproving earlier claims (*25*). The process for single-photon emission from a given donor under these pumping conditions is likely nonresonant photoionization from the singly ionized charge state to the doubly ionized charge state, followed by cascade recapture of the resulting free electron. After a phonon cascade (*26*) to 1s:Γ_7, the electron then emits a photon as it transitions to the ground state. Resonantly pumping higher excited orbital states ought to give rise to a similar cascade/emission process. Electrical injection techniques (*27*) could be used to generate these single photons on demand.

With known concentrations and absorption coefficients, we calculate an upper bound for the radiative lifetime of this zero-phonon transition to be 39 μs, giving a transition dipole moment of at least 0.77 D (see the Supplementary Materials). The Lorentzian line shapes seen in Fig. 1 (D and E) might have suggested a homogeneous, lifetime-limited process, but the spectra of a second sample having identical isotopic composition, although with a much higher (1×10^{15} cm^{-3}) concentration of the acceptor boron, also showed Lorentzian line shapes but with a considerably greater linewidth of 0.022 cm^{-1} (2.7 μeV) (fig. S1). This demonstrates the importance of inhomogeneous broadening in the observed spectral line shapes, and we have performed spectral hole-burning experiments (see Materials and Methods and the Supplementary Materials) revealing a resolution-limited homogeneous linewidth of at most 0.12 μeV (29 MHz), corresponding to an excited-state lifetime of at least 5.5 ns.

The remaining discrepancy between the bound on the homogeneous linewidth provided by the spectral hole-burning and the radiative lifetime determined from the no-phonon absorption strength is unlikely to be purely due to nonradiative recombination processes. In this system, Auger decay processes do not apply. The 1s:A ⇔ 1s:Γ_7 splitting amounts to seven (or more) phonon energies, making multiphonon cascade an improbable decay path. We do not observe any indication of subunit radiative efficiency through, for example, visible phonon sidebands, in agreement with previous absorption studies (*21*), although, of course, weak phonon-assisted sidebands remain a possibility. The characterization of the actual excited-state lifetime, possible dephasing processes, and radiative efficiency will be the subject of future study.

The spin-valley hybridization of the 1s:Γ_7 states gives rise to an optical Λ transition with efficient dipole matrix elements between all 1s:A and 1s:Γ_7 electronic states. We apply resonant (either S ⇔ 1s:Γ_7 or T ⇔ 1s:Γ_7) laser excitation to these Λ transitions to generate hyperpolarization for singlet-triplet spin qubit initialization. Here, hyperpolarization means the generation of spin polarization far beyond what can be achieved under thermal equilibrium conditions. As shown in Fig. 1E, we achieve near-unit polarization of all spins in the bulk using 4 μW of resonant laser light with a 50 ms time constant.

With the sample mounted in a split-ring resonator (fig. S2), we observe magnetic resonance transitions from the singlet state S_0 to the triplet states $\{T_+, T_0, T_-\}$, optically detected via the relative absorption of the T ⇔ 1s:Γ_7 transition (Fig. 2, A and B). As with ^{31}P (*28*), the S_0 ⇔ $T_\pm$ transitions are more efficient than the S_0 ⇔ T_0 transition when B_0 (Earth's field) is perpendicular to B_1, the resonant radio frequency (rf) driving field (see the Supplementary Materials).

We confirm that the S_0 ⇔ T_0 qubit is long-lived by performing both T_1 relaxation and T_2 spin-echo measurements. Initial measurements show that $T_1 \approx 2$ s (fig. S2), which we extend beyond 6 min (Fig. 2C) with the addition of cold optical sample shielding, indicating that room temperature blackbody radiation entering through the dewar windows is a dominant driver of T_1 relaxation in this spin system (see the Supplementary Materials).

The S_0 ⇔ T_0 qubit in Earth's magnetic field (Fig. 2A) is near a magnetic field "clock transition" where $df/dB = 0$ (where f is the transition frequency and B is the magnetic field), removing a first-order

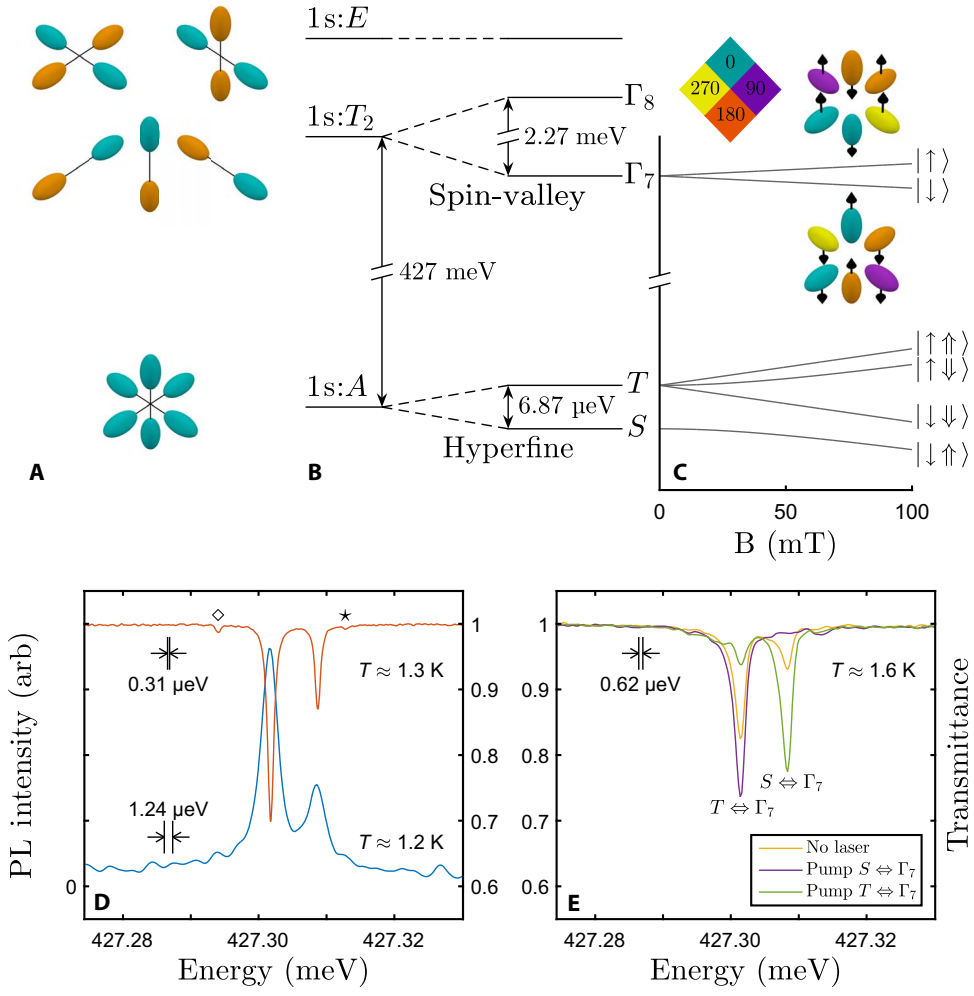

Fig. 1. Orbital levels of ^{28}Si:^{77}Se^{+}. (**A**) Valley composition of the six sublevels of the 1s hydrogenic manifold of ^{28}Si:^{77}Se^{+}, ignoring spin interactions. (**B**) With electron spin interactions, the six 1s:T_2 levels are split into 1s:Γ_7 (two states) and 1s:Γ_8 (four states) by the spin-valley interaction. With nuclear spin interactions, the 1s:A states are split by the hyperfine interaction into electron-nuclear spin singlet S_0 and triplet $\{T_-,T_0,T_+\}$ states (not to scale). (**C**) These eigenstates change according to an applied magnetic field. The spin-valley composition of the 1s:Γ_7 states in a magnetic field are shown with spin (anti) alignment with the background magnetic field indicated by arrows and valley phase indicated by color. In the high-field limit, the 1s:A and 1s:Γ_7 states are labeled according to nuclear spin (⇑,⇓) and electron spin (↑,↓). (**D**) Transmission spectra (top) and photoluminescence (PL) spectra (bottom) collected with different resolutions as indicated. The small side peaks (◦ and ⋆) are because of small concentrations of ^{76}Se^{+} and ^{78}Se^{+}, respectively. (**E**) Unpolarized (yellow) and singlet/triplet hyperpolarized (green and purple, respectively) transmission scans of the 1s:A ⇔ 1s:Γ_7 optical transitions (see main text).

sensitivity to magnetic field fluctuations (*29*, *30*). Performing a spin-echo measurement (B_0 = 70 μT) (Fig. 3A and fig. S3), we measure T_2 = 2.14 ± 0.04 s using a single π-pulse sequence, which is longer than reported electron Hahn-echo times collected away from a clock transition (*31*), as expected. These clock transition T_2 times are extended using two-, four-, and eight-pulse alternating Carr-Purcell-Meiboom-Gill (CPMG) sequences (Fig. 3A bottom-left inset and fig. S4), indicating that low-frequency fluctuations (such as residual XX + YY dipolar coupling terms or hydrostatic pressure variations) are responsible for spin dephasing (see the Supplementary Materials). From tip-angle measurements [Fig. 3A (top right inset) and the Supplementary Materials] (*30*), we confirm a ^{77}Se^{+} concentration upper bound of 2.1 × 10^{13} cm^{-3}.

Strategy

This photonically active, long-lived spin qubit candidate is well-suited to a cavity QED qubit coupling architecture using CMOS-compatible silicon photonic structures. Hybrid photonic cavity QED approaches have been proposed using nitrogen-vacancy centers in diamond (*32*–*34*), group III-V quantum dots (*35*–*37*), and silicon carbide (*38*), yet the fabrication and optical/spin characteristics of ^{77}Se^{+} implanted into a silicon platform make it an attractive candidate. It has previously been shown that impurities, such as Al, Ga, and In, can be introduced into ^{28}Si by ion implantation followed by thermal annealing while retaining the large spectroscopic advantages that ^{28}Si has over natural Si (*39*).

Strong coupling between a donor and a silicon-on-insulator (SOI) photonic crystal cavity can be achieved by implanting ^{77}Se^{+} ions into the mode maximum of a cavity with a resonance frequency matching particular 1s:A ⇔ 1s:Γ_7 optical transitions. The charge state can be set using, for example, electron/hole injection techniques (*27*). Because of the long wavelength, this mode maximum is a few hundred nanometers away from interfaces, and so, implanted donors will preserve their bulk-like spin and optical characteristics (Fig. 4, A and B, for an "L3" cavity manifestation). Implantation straggle at these target depths is smaller

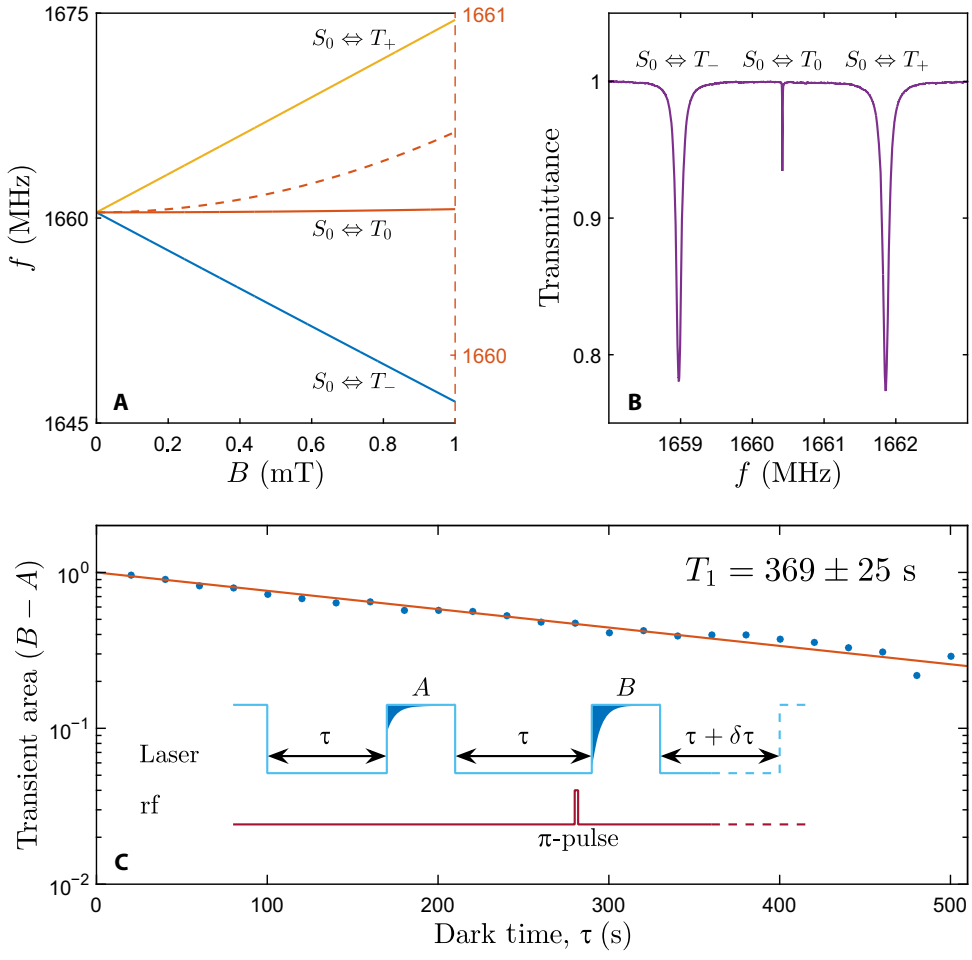

Fig. 2. Singlet ⇔ triplet magnetic resonance of $^{77}Se^+$ in Earth's magnetic field. (**A**) Frequencies of the singlet ⇔ triplet transitions as a function of magnetic field *B*. The $S_0 \Leftrightarrow T_\pm$ transitions vary linearly with *B*, whereas the $S_0 \Leftrightarrow T_0$ transition is first-order insensitive to changes in *B*, giving rise to a quadratic clock transition (see text). A *y*-axis magnification of the $S_0 \Leftrightarrow T_0$ transition is displayed with a dashed line, corresponding to the right dashed *y* axis. (**B**) Magnetic resonance spectra, as a function of B_1 frequency, measured via the change in triplet absorption after hyperpolarization, were taken at $T = 2.0$ K. All three singlet ⇔ triplet transitions are well resolved in Earth's magnetic field (here, 70 μT). (**C**) Measured polarization decay showing the relaxation time constant, T_1, to be over 6 min at $T = 1.2$ K. Inset: Pulse sequence used to measure T_1. For each wait duration τ, polarization was measured as the difference between two integrated absorption transients, one with (*B*) and one without (*A*) a leading population inversion π pulse. These absorption transients also served to fully reinitialize the $S_0 \Leftrightarrow T_0$ qubit ensemble.

(~80 nm depth, ~50 nm lateral) than $\lambda/2n$ (~425 nm). We anticipate less than 10% standard deviation in donor-cavity coupling strength from implantation straggle and acknowledge that more precise placement techniques could be used if necessary. With a transition dipole moment of 0.77 D and an "L3" cavity volume of $(\lambda/n)^3$, we calculate a vacuum Rabi splitting of $2g = 2\pi \times 190$ MHz (see the Materials and Methods), which is larger than the upper bound for the 1s:$A \Leftrightarrow$ 1s:Γ_7 homogeneous linewidth (29 MHz). Nonradiative or phonon-assisted decay may be reduced, for example, through density of states engineering. Cavity *Q* factors on the order of 10^5 will be required to obtain strong coupling.

The Jaynes-Cummings "ladder" (*40*) for a coupled cavity-chalcogen donor system is given in Fig. 4C, where a nuclear spin-zero isotope was chosen for clarity. In the absence of an applied magnetic field, the standard on-resonance Jaynes-Cummings ladder of states applies (shown in orange). The orientation of an applied magnetic field may be chosen to maximize optical coupling with the chosen cavity mode, for example, a linearly polarized TE cavity. When a magnetic field is applied (shown in blue), the ground and excited spin states split with differing *g*-factors (*15*), and the excited-state levels are no longer resonant. To tune back into resonance, the 1s:Γ_7 excited states can be dynamically adjusted through the application of electric fields or strain (to be discussed shortly). The resulting strong-coupling condition is then spin-dependent.

Spin-dependent cavity coupling will allow for efficient single-shot single-spin readout near 4.2 K without optical excitation of the donor, as follows (Fig. 4, C and D). In the event that the electron spin is in the uncoupled (for example, up) ground state (red trace), the cavity will preferentially transmit any light matching the bare cavity frequency (or reflect, depending on how light is coupled to the cavity) (*41*–*43*). A large number of photons can be used to infer the cavity response without exciting the nonresonant donor transition (*33*). In the event that the electron spin is in the coupled (for example, down) ground state (green trace), the cavity will become strongly coupled and will no longer respond to the bare uncoupled optical frequency; instead, resonant light will now preferentially reflect from the cavity. Again, a large number of photons can be used to infer this distinct spin-dependent cavity response, without exciting the nonresonant coupled cavity-donor transitions. In the strong-coupling regime, coupling strength variations on the

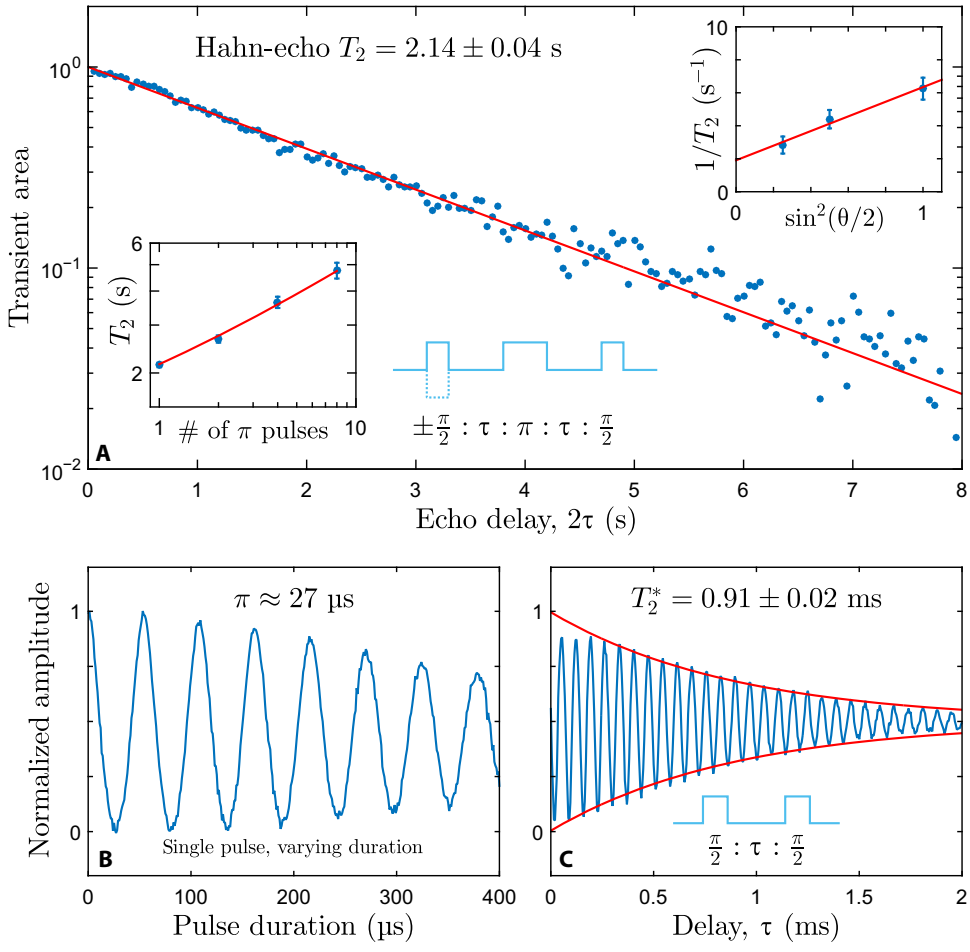

Fig. 3. Spin coherence properties of $^{77}Se^+$. (**A**) Center: Hahn-echo T_2 measurements with rf pulse sequence (inset) showing a coherence time of 2.14 ± 0.04 s at T = 1.2 K, collected with a phase-cycled leading π/2 pulse and varied τ. (A) Top right: Varying the amount of rotation in the refocusing pulse of a Hahn-echo experiment (a tip-angle measurement) can be used to deduce the concentration of the sample. We confirm a $^{77}Se^+$ concentration upper limit of 2×10^{13} cm^{-3} under these experimental conditions. (A) Bottom left: These Hahn-echo times can be extended with dynamic decoupling sequences. We see square-root extension of coherence times as a function of N, the number of refocusing pulses, here applied as an alternating CPMG sequence (see main text). (**B**) Rabi oscillations of the $S_0 \Leftrightarrow T_0$ qubit ensemble. (**C**) Ramsey fringes of the $S_0 \Leftrightarrow T_0$ qubit ensemble. The fitted envelope (red) gives a T_2^* value of approximately 1 ms, arising from static magnetic field inhomogeneities.

order of 10% will not appreciably affect the fidelity of this readout mechanism. Inferring the spin state through single-photon emission is also a possibility using integrated high-efficiency superconducting nanowire single-photon detectors (*44*). In the few-photon regime, photon blockade effects (*45*–*48*) could also be used to infer the spin state of the system.

For $^{77}Se^+$, a nuclear spin clock transition exists near 1.73 T, and the differing g-factors in the 1s:A and 1s:Γ_7 manifolds mean that electron spin–selective optical transitions at this field are separated by tens of gigahertz (many tens of microelectron volts) (*15*). A qubit could be stored within the uncoupled clock-transition nuclear spin state, globally manipulated using magnetic resonance (which are compatible with photonic devices) and coupled/measured via the electron spin–selective cavity-coupled optical transitions.

Uniaxial strain and electric fields will have a negligible perturbative effect on the resonant frequencies of the 1s:A spin states because the first excited state is 427.3 meV higher in energy. Hydrostatic pressure can shift the hyperfine value only slightly (see the Supplementary Materials). In contrast, strain (*20*), magnetic field (*15*), and electric field (*18*, *19*) can all be used to tune the eigenstates and energies of the 1s:Γ_7 states, which are energetically close to the 1s:Γ_8 and 1s:E levels. This has two positive implications. First, this ground-state insensitivity will be vital for the spin qubits' uniformity and for the preservation of ultralong lifetimes in a device. If selective spin frequency control is necessary, then hydrostatic pressure (*49*) or electrical control of the quadrupole moment (*50*) of the spin-$^3/_2$ isotope $^{33}S^+$ can be used. Second, electric fields or strain can be used to tune the optical transition frequencies of individual donors. This can be used to compensate for photonic cavity frequency mismatch; the resonant frequencies of SOI photonic cavities are relatively fixed at a given temperature and display some manufacturing variability. These tuning capabilities offer the prospect of dynamically adjusting the donors' optical frequencies for selective control and coupling, without compromising the long-lived spin qubit ground states.

These spin-selective optical transitions broaden above 4.2 K by thermal activation into 1s:Γ_8 (fig. S5). Higher-temperature operation may be possible by using a highly strained substrate, which not only repopulates the states' spin-valley composition but also shifts their excited-state splittings (*51*). From a decoherence perspective, the thermal density of states matching the 1s:$A \Leftrightarrow$ 1s:Γ_7 optical transition is negligible at 4.2 K. Even a high Q cavity's amplification of the density

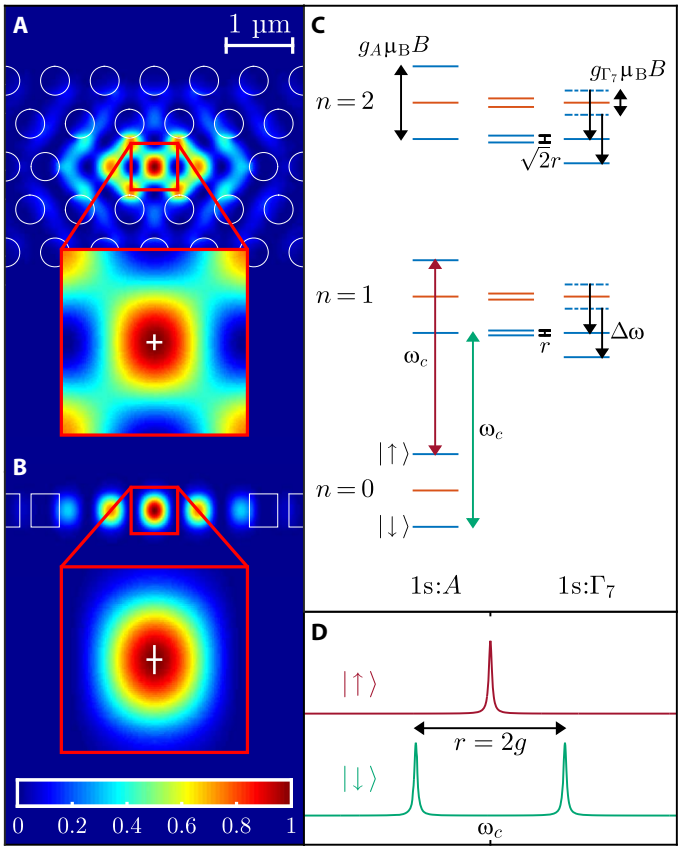

Fig. 4. Coupled cavity-donor system. (**A**) Simulated electric field intensity of a silicon photonic L3 cavity mode at ~427.3 meV (2902 nm), viewed top-down, modeled after the work of Shankar *et al.* (*63*). Inset: Fourfold magnification of the mode maximum region. The white crosshair indicates the calculated lateral implantation straggle. (**B**) Cross-sectional view of the long axis of the same 0.5 μm thick photonic L3 cavity mode at ~427.3 meV (2902 nm). Inset: Fourfold magnification of the mode maximum region with indicated implantation straggle. (**C**) The Jaynes-Cummings ladder of available energy eigenstates in a single chalcogen-cavity coupled system. At zero field, with a zero nuclear spin isotope and the cavity frequency, ω_c, on resonance with the 1s:A ⇔ 1s:Γ_7 transition, the regular ladder of states exists (orange). With an applied magnetic field (blue), the ground-state electron states split according to g_A = 2.0057 and the excited state splits according to $g_{\Gamma 7}$ = 0.644. Detuning the 1s:Γ_7 excited state ($\Delta\omega$) with, for example, electric fields, brings these excited-state levels into alignment to observe spin-dependent strong coupling r. (**D**) Calculated spin-dependent strong coupling of the donor-implanted L3 cavity, neglecting cavity losses: Only one spin state (bottom) has a split optical spectrum near the bare cavity frequency.

of states at the 1s:A ⇔ 1s:Γ_7 optical frequency is expected to result in a negligible enhancement of spin decoherence. Consequently, this cavity QED scheme will (i) avoid Purcell decoherence of the qubits and (ii) not contribute significantly to an Orbach or Raman indirect spin relaxation process (*24*). Nevertheless, dynamically detuning the optical frequency will remain available, which may prove useful for tasks such as triggered photon emission.

This platform can be used to scale to large networks of entangled qubits in a number of ways. By way of example, we propose a particular approach that is motivated by the favorable error thresholds and modularity of a networked (*52*) quantum architecture. Each module will consist of a small number of nearby coupled [~$(\lambda/n)^3$] optical cavities with donors implanted into each distinct mode maxima. These "photonic molecules" have been realized experimentally (*53*). Each donor's optical frequencies can be tuned with nearby electrodes or piezoelectrics. User-defined frequency detunings will result in distinct, conditional excitation spectra for a given donor, and each donor will be able to undergo independent readout through a coupled waveguide.

A number of entangling operations would be possible in this configuration. Geometric rotations through these excited states can impart conditional phase gates (*54*) upon ground-state spins through pulsed optical resonance. Similarly, parity measurements of distinct spins can be performed by measuring the combined effect that multiple cavity-donor systems have upon a photon traveling through a nearby coupled waveguide. The 1s:A ⇔ 1s:Γ_7 states form a Λ transition with similar decay rates, and a resonant single photon could be used to deterministically drive a conditional, and perhaps virtual, Raman transition (*43*, *55*). Any of these operations, plus global single-qubit operations, are sufficient for universality within a single module. Many other coupling approaches (*33*, *56*–*58*) developed in the context of cavity QED also apply.

Modules can be linked optically. Strong coupling can be used to generate entanglement between the path of passing photons and the electron spin state. Moreover, single donors within a module can be made to emit photons through targeted pulsed hole and electron injection (*27*). The polarization and frequency of a photon emitted as an electron moves from 1s:Γ_7 →1s:A will, in general, be frequency- and polarization-entangled with the remaining spin qubit state. Strong cavity coupling will, in general, change the frequency and effective radiative lifetime of these otherwise spectrally indistinguishable emitters. Triggered single photons can be coupled into a nearby waveguide, and parity measurements between multiple waveguided photons can be used to entangle emitters from distinct modules, both within and between devices (*59*). This entanglement need not be particularly pure (*52*); the other donors present in each module can be used to swap and purify a poor initial distributed entangled state. Cluster states (*60*) could be constructed from these building blocks.

CONCLUSION AND OUTLOOK

We have proposed a new method of measuring and coupling donor spin qubits in silicon by exploiting the parity-allowed optical transitions of singly ionized deep donors in silicon within photonic cavity QED devices. We have shown that these transitions emit light and that their spin ground states are long-lived near 4.2 K. This CMOS-compatible platform does not rely upon milliKelvin temperatures, large magnetic fields, or interface charge dynamics. Using this strategy, the spin qubits will preserve their bulk-like decoherence properties, and the readout and coupling mechanisms will be robust to the variations in strains and electric fields present in realistic devices.

These silicon-integrated emitters will enable a number of other photonic and quantum technologies, such as quantum repeaters, fast all-optical switches (both classical and quantum), silicon-based optical sources, and more. A number of intriguing variants could be pursued, including other mid-IR transitions using the chalcogens' neutral charge states, nuclear spin–free isotopes for more spectrally uniform photonic emission, engineered superradiant effects, photon conversion to communication wavelengths, spin (microwave) to mid-IR photon conversion, chiral cavity coupling, and adaptations of these strategies to natural silicon.

MATERIALS AND METHODS

Apparatus

Two lasers were used in this study. The PL measurements used a 1147 meV (1081 nm) distributed feedback (DFB) Yb-doped fiber laser followed by a Yb-doped fiber amplifier emitting a maximum of 1 W. All other studies used a narrow-linewidth 427.3 meV (2902 nm) DFB laser diode (nanoplus GmbH) emitting ~3 mW, where a small part of the laser power was directed to a wavemeter (Bristol Instruments 621A-IR) for wavelength tracking and feedback (±0.2 ppm absolute accuracy). To tune this DFB laser to specific wavelengths, wavelength scans were performed by sweeping the drive current in 100 μA steps, corresponding to wavelength shifts of ~1.6 μeV per step. Fine-tuning of the laser wavelength was achieved by applying a small voltage to the external current modulation input of the laser controller.

Transmission and PL spectra were collected using a Bruker IFS 125HR Fourier transform infrared (FTIR) spectrometer with gold mirrors and a CaF_2 beamsplitter. The FTIR transmission measurements used a Globar source and a liquid nitrogen–cooled InSb detector, whereas the PL measurements were detected using a liquid nitrogen–cooled InAs detector.

Optical bandpass filters (Spectrogon) were used to limit incident light on the FTIR detectors to a narrow (~55 or ~130 nm) region around the desired wavelengths. This was important because most of the spectrum was outside the region of interest and thus contributed solely to the noise level. Blocking these regions greatly enhanced the signal-to-noise ratio of the spectrum in the region of interest, which was particularly important for the highest spectral resolution scans. We note that the 1s:*A* to 1s:Γ_7 absorption could still be observed without using these bandpass filters and even when using the unfiltered quartz-halogen NIR source, although with reduced signal-to-noise ratio and a somewhat reduced absorption strength due to photoneutralization of $^{77}Se^+$ resulting from the free electrons (and holes) generated by the above bandgap light.

All FTIR spectra shown here were obtained using a three-term Blackman-Harris apodization function and a zero-filling factor of four. For the $^{77}Se^+$ 1s:*A* ⇔ 1s:Γ_7 absorption transitions, this gave an observed full width at half maximum (FWHM) linewidth of 1.0 μeV (0.008 cm^{-1}). Retransforming the same interferogram using "boxcar" apodization, resulted in a somewhat noisier spectrum with a 100% Lorentzian fit, having a FWHM of 0.87 μeV (0.007 cm^{-1}). Undoped silicon has no absorption features anywhere near these chalcogen transitions, therefore correction for this was not necessary. However, there are water vapor absorption lines present in the instrumental response function near the $^{77}Se^+$ transitions (but not in the region covered in Fig. 1 and fig. S1), and these were corrected by dividing the sample spectra with reference spectra collected under the same conditions but without the presence of a sample.

For measurements requiring temperatures above 4.2 K, a Lake Shore 805 temperature controller connected to a heater on the sample holder was used to maintain the sample at a fixed temperature with cooling provided by flowing cold He gas. At all temperatures, rf was coupled to the sample via a split ring resonator formed on a Pyrex tube and tuned to the zero-field hyperfine splitting (1.66 GHz or 6.87 μeV) and coupled to the rf source by a coupling loop.

Pulsed measurements

For rf pulsed measurements (for example, T_1 and T_2), the DFB laser and microwave source were both gated using a SpinCore PulseBlaster. The laser, tuned to, for example, the $T \Leftrightarrow \Gamma_7$ transition, was sent through a shutter (SRS SR475), through a liquid helium cryostat containing the sample and into a liquid nitrogen–cooled InAs detector, whose output was connected to a signal-averaging oscilloscope (fig. S2A). The 1.66 GHz microwaves driving the split ring resonator were gated by a microwave switch.

Spins were prepared optically using one of the pumping schemes shown in Fig. 1E, and following this, pulsed rf measurements were taken with the shutter closed. At the conclusion of a given sequence of microwave pulses, the shutter was opened and a transient optical absorption was recorded on the oscilloscope. The amount of $T \Leftrightarrow \Gamma_7$ laser light initially arriving at the detector was used to infer the population of spins in the *T* spin states: For example, a larger absorption indicated a greater number of spins in the *T* state because spins in the singlet state were optically off-resonance. Absorption traces decayed to a baseline value as all optically resonant spins were pumped into a nonresonant spin state via excitation into 1s:Γ_7. This entire transient area was used to extract a higher signal-to-noise estimate of the spin state per pulse sequence measurement.

The baseline value for a given transient is proportional to the sum of all photons, which are incident upon the liquid nitrogen–cooled InAs detector during the detection period, including, for example, ambient scattered light. To extract a meaningful result free of this large background signal, we adopted rf phase-cycling techniques. Phase-cycling works by comparing the results of multiple near-identical iterations of a given pulse sequence, where only the phases of particular pulses are changed, and by subtracting the results to cancel backgrounds. In the example of a Hahn echo, as shown in the inset of Fig. 3A, the first π/2 pulse is two-step phase-cycled with a phase of either ±*x*. These two sequences result in reversed spin populations in the spin basis. The difference between the two resulting transients is directly proportional to the signal of interest, and correspondingly, this difference is the transient area referred to in the main text.

Phase-cycling was adopted in nearly all pulsed rf measurements. In the case of all T_1 measurements, phase-cycling was applied with two adjacent π/2 pulses where the first π/2 pulse had a phase of ±*x* and the second pulse had a phase of +*x*. This had the result shown in the inset Fig. 2C, where the π pulse in the second sequence corresponds to two +*x* π/2 pulses, and the absent π pulse in the first sequence corresponds to a –*x* π/2 pulse followed by a +*x* π/2 pulse. We compared the difference in transients with and without an applied π pulse, but this phase-cycled approach removed possible sources of error from applying different amounts of microwave power in the two different sequences. Similarly, all phase-cycling experiments were performed automatically after one another, shot by shot, to reduce sources of error due to any possible drift of environmental parameters. The maximum transient area, corresponding to the difference in transients between fully polarized *T* and *S* states, was assigned a polarization value of 1, reflecting the initial polarization seen in Fig. 1E. Normalized results, specifically the Rabi and Ramsey measurements in Fig. 3 (B and C), were not phase-cycled, and so a simple baseline subtraction and normalized contrast was applied in these cases.

Spectral hole burning

Spectral hole burning can reveal the homogeneous linewidth of an inhomogeneously broadened ensemble line shape by "burning a hole" in the inhomogeneous population using a fixed laser frequency and then measuring the resulting absorption profile, in our case, using the FTIR spectrometer. In this situation, the hole results from removing population from within a homogeneous linewidth of the laser frequency, which

for concreteness could be set near the peak of the T absorption line, and moving that population to the S state separated in energy by the hyperfine value A, resulting in excess population, or an "anti-hole," at that energy. In the limit of low pump laser power (small hole depth), the observed features in our hole burning measurement (fig. S1) were a convolution of a Lorentzian having twice the homogeneous linewidth (*61*), the laser line shape, and the inherent resolution and line shape of the FTIR spectrometer. To account for these instrumental contributions, a spectrum of the laser was collected with the FTIR under identical conditions and found to have a Gaussian profile with a FWHM of 0.23 μeV. This line shape is a convolution of the inherent resolution of the FTIR spectrometer and the line shape of the laser.

To extract the actual linewidths of the hole and antihole, we fit them to a Gaussian with a FWHM of 0.23 μeV convolved with an adjustable Lorenztian. The FWHM of the best-fit Lorentzian was found to be 0.24 μeV, which places an upper bound of 0.12 μeV on the homogeneous linewidth of the 1s:$A \Leftrightarrow$ 1s:Γ_7 transitions (*61*). Note that these are resolution-limited values.

Samples

The silicon sample used for all measurements shown in the main text was enriched to 99.991% ^{28}Si, contained 75-ppm ^{29}Si and ~5×10^{13} cm^{-3} boron, and had dimensions of 2 mm × 2 mm × 10 mm, with the optical path along the long axis. After the ^{77}Se diffusion at 1200 C for 1 week, the sample was n-type, with ~2×10^{13} cm^{-3} ^{77}Se$^+$ (see below), which is at least 10 times higher than the concentration of ^{77}Se^0.

The singly ionized ^{77}Se donor concentration was calculated via the slope of the fit to the tip-angle Hahn-echo data, taken using the $S_0 \Leftrightarrow T_+$ transition, shown in the upper right inset of Fig. 3A. This relation is given by Wolfowicz *et al.* (*30*)

$$\frac{1}{T_{2,\mathrm{Hahn}}} = \frac{1}{T_{2,\mathrm{Int}}} + [^{77}\mathrm{Se}^+]\,(2\pi\gamma_{\mathrm{eff}})^2\,\frac{\pi}{9\sqrt{3}}\mu_0\hbar\,\sin^2(\theta/2)$$

where μ_0 is the permeability of free space, $\gamma_{\mathrm{eff}} = df/dB = 14.036$ GHz/T is the $S_0 \Leftrightarrow T_+$ transition's frequency sensitivity as a function of magnetic field, $\hbar$ is the reduced Planck constant, $[^{77}\mathrm{Se}^+]$ is the donor concentration per m^3, and θ is the angle in radians used in the tip-angle Hahn-echo pulse sequence $\frac{\pi}{2}$:τ:θ:τ:$\frac{\pi}{2}$. Given a slope of 4.4 extracted from the upper right inset of Fig. 3A, we calculated ^{77}Se$^+ = 2.1 \times 10^{13}$ cm^{-3}. This concentration estimate is an upper bound when applied to the entire sample because the donors are not uniformly distributed. On the basis of the duration and temperature profile of the diffusion scheme used, we estimated that the selenium diffuses a few tenths of a millimeter into the 2 mm × 2 mm × 10 mm sample. Higher-concentration regions of the sample near the surfaces, where most of the donors are located, will contribute significantly to tip-angle measurements. The optical absorption spectra seen in Fig. 1 (D and E) will have contributions from the substantially lower-concentration center of the sample. This would result in less optical absorption compared to a sample doped uniformly at the 2.1×10^{13} cm^{-3} level, which is why we gave the estimate of the dipole moment of 0.77 D only as a lower bound.

For the spectral hole-burning measurements, a second ^{28}Si sample having the same 99.991% isotopic enrichment, but a higher boron concentration of 1×10^{15} cm^{-3}, was diffused with ^{77}Se using the same procedure as for the first sample. The stronger ^{77}Se$^+$ absorption and somewhat broader linewidths of this sample made the resulting spectral hole and antihole easier to observe.

Transition dipole moment and radiative lifetime calculations

For the purposes of calculating lower/upper bounds for the transition dipole moment and radiative lifetime, we will assume a uniform concentration of ^{77}Se$^+ = 2.1 \times 10^{13}$ cm^{-3}.

Given an integrated absorption cross section and sample concentration, the radiative decay time of a particular transition is given by Hilborn (*62*)

$$\tau = \frac{g_2}{g_1}\frac{\lambda^2}{8\pi n^2 \int \alpha dV} \quad (1)$$

where g_1 and g_2 are the degeneracy of the 1s:A and 1s:Γ_7 states, respectively, λ is the wavelength in centimeters, n is the index of refraction at λ, and $\int \alpha dV$ is the integrated absorption cross section in square centimeters per second. Here, we have $g_1 = g_2$ as 1s:A and 1s:Γ_7, each contain two electronic states.

For the $T \Leftrightarrow$ 1s:Γ_7 "triplet" transition, a purely Lorentzian peak with a peak-normalized transmission of 0.70, a sample length of 1.0 cm, and a FWHM of 0.87 μeV ≈ 210 MHz, a lower bound on the integrated absorption cross section, is given by

$$\frac{\ln(0.70)}{1.0\ \mathrm{cm}} \times \frac{\pi}{2} \times \frac{2.1 \times 10^8\ \mathrm{s}^{-1}}{2.1 \times 10^{13}\ \mathrm{cm}^{-3}} = 5.6 \times 10^{-6}\ \mathrm{cm/s}$$

To include the $S \Leftrightarrow$ 1s:Γ_7 "singlet" transition in the total integrated cross section, we multiplied the above value by $\frac{4}{3}$ to account for the singlet/triplet degeneracies. This gave a total of $\int \alpha dV = 7.5 \times 10^{-6}$ cm^2 s^{-1}. With this value, we evaluated Eq. 1 to extract a radiative lifetime upper bound of τ ≈ 39 μs. From the variable donor concentration profile, we know that this is an overestimate of the true radiative lifetime, perhaps by a factor of 2 or more.

Using a radiative lifetime of τ ≈ 39 μs, we calculated (*62*) a minimum transition dipole moment of

$$\mu = \sqrt{\frac{3\varepsilon_0\varepsilon_r h(c/n)^3}{2\omega^3\tau}} = 2.6 \times 10^{-30}\ \mathrm{cm} \approx 0.77\ \mathrm{D}$$

where ω is the angular frequency of the transition, ε_0 is the permittivity of free space, $\varepsilon_r = 11.68$ is the relative permittivity of silicon, h is Planck's constant, c is the speed of light, and $n = 3.4$ is the refractive index of silicon at 427.3 meV.

From this and an assumed cavity volume of $V = (\frac{\lambda}{n})^3$, we calculated a splitting of

$$2g = 2\mu\sqrt{\frac{\omega}{2\hbar\varepsilon_0\varepsilon_r V}} = 2\pi \times 190\ \mathrm{MHz}$$

SUPPLEMENTARY MATERIALS

Supplementary material for this article is available at http://advances.sciencemag.org/cgi/content/full/3/7/e1700930/DC1

Hyperfine constant

T_1 decoherence

T_2 decoherence

fig. S1. Linewidth measurements using hole burning.

fig. S2. Impact of room temperature blackbody radiation on T_1 lifetimes.
fig. S3. Illustration of phase noise on and off the clock transition.
fig. S4. T_2 coherence time scaling with number of π pulses.
fig. S5. Temperature dependence of the 1s:A ⇔ 1s:Γ7 optical transitions' linewidth.
Reference (*64*)

REFERENCES AND NOTES

1. K. Saeedi, S. Simmons, J. Z. Salvail, P. Dluhy, H. Riemann, N. V. Abrosimov, P. Becker, H.-J. Pohl, J. J. L. Morton, M. L. W. Thewalt, Room-temperature quantum bit storage exceeding 39 minutes using ionized donors in silicon-28. *Science* **342**, 830–833 (2013).
2. G. Wolfowicz, A. M. Tyryshkin, R. E. George, H. Riemann, N. V. Abrosimov, P. Becker, H.-J. Pohl, M. L. W. Thewalt, S. A. Lyon, J. J. L. Morton, Atomic clock transitions in silicon-based spin qubits. *Nat. Nanotechnol.* **8**, 561–564 (2013).
3. J. T. Muhonen, A. Laucht, S. Simmons, J. P. Dehollain, R. Kalra, F. E. Hudson, S. Freer, K. M. Itoh, D. N. Jamieson, J. C. McCallum, A. S. Dzurak, A. Morello, Quantifying the quantum gate fidelity of single-atom spin qubits in silicon by randomized benchmarking. *J. Phys. Condens. Matter* **27**, 154205 (2015).
4. J. P. Dehollain, S. Simmons, J. T. Muhonen, R. Kalra, A. Laucht, F. Hudson, K. M. Itoh, D. N. Jamieson, J. C. McCallum, A. S. Dzurak, A. Morello, Bell's inequality violation with spins in silicon. *Nat. Nanotechnol.* **11**, 242–246 (2015).
5. B. E. Kane, A silicon-based nuclear spin quantum computer. *Nature* **393**, 133–137 (1998).
6. S. R. Schofield, N. J. Curson, M. Y. Simmons, F. J. Rueß, T. Hallam, L. Oberbeck, R. G. Clark, Atomically precise placement of single dopants in Si. *Phys. Rev. Lett.* **91**, 136104 (2003).
7. B. Koiller, X. Hu, S. Das Sarma, Exchange in silicon-based quantum computer architecture. *Phys. Rev. Lett.* **88**, 027903 (2001).
8. G. Tosi, F. A. Mohiyaddin, H. Huebl, A. Morello, Circuit-quantum electrodynamics with direct magnetic coupling to single-atom spin qubits in isotopically enriched ^{28}Si. *AIP Adv.* **4**, 087122 (2014).
9. G. Tosi, F. A. Mohiyaddin, V. Schmitt, S. Tenberg, R. Rahman, G. Klimeck, A. Morello, Silicon quantum processor with robust long-distance qubit couplings. http://arxiv.org/abs/arxiv:1509.08538 (2015).
10. P. T. Greenland, S. A. Lynch, A. F. G. van der Meer, B. N. Murdin, C. R. Pidgeon, B. Redlich, N. Q. Vinh, G. Aeppli, Coherent control of Rydberg states in silicon. *Nature* **465**, 1057–1061 (2010).
11. M. L. W. Thewalt, A. Yang, M. Steger, D. Karaiskaj, M. Cardona, H. Riemann, N. V. Abrosimov, A. V. Gusev, A. D. Bulanov, I. D. Kovalev, A. K. Kaliteevskii, O. N. Godisov, P. Becker, H. J. Pohl, E. E. Haller, J. W. Ager III, K. M. Itoh, Direct observation of the donor nuclear spin in a near-gap bound exciton transition: ^{31}P in highly enriched ^{28}Si. *J. Appl. Phys.* **101**, 081724 (2007).
12. M. Steger, K. Saeedi, M. L. W. Thewalt, J. J. L. Morton, H. Riemann, N. V. Abrosimov, P. Becker, H.-J. Pohl, Quantum information storage for over 180 s using donor spins in a ^{28}Si "semiconductor vacuum". *Science* **336**, 1280–1283 (2012).
13. M. Abanto, L. Davidovich, B. Koiller, R. L. de Matos Filho, Quantum computation with doped silicon cavities. *Phys. Rev. B* **81**, 085325 (2010).
14. M. J. Gullans, J. M. Taylor, Optical control of donor spin qubits in silicon. *Phys. Rev. B* **92**, 195411 (2015).
15. M. Steger, A. Yang, M. L. W. Thewalt, M. Cardona, H. Riemann, N. V. Abrosimov, M. F. Churbanov, A. V. Gusev, A. D. Bulanov, I. D. Kovalev, A. K. Kaliteevskii, O. N. Godisov, P. Becker, H.-J. Pohl, E. E. Haller, J. W. Ager III, High-resolution absorption spectroscopy of the deep impurities S and Se in ^{28}Si revealing the ^{77}Se hyperfine splitting. *Phys. Rev. B* **80**, 115204 (2009).
16. H. G. Grimmeiss, E. Janzén, K. Larsson, Multivalley spin splitting of **1*s*** states for sulfur, selenium, and tellurium donors in silicon. *Phys. Rev. B* **25**, 2627 (1982).
17. H. G. Grimmeiss, E. Janzén, H. Ennen, O. Schirmer, J. Schneider, R. Wörner, C. Holm, E. Sirtl, P. Wagner, Tellurium donors in silicon. *Phys. Rev. B* **24**, 4571 (1981).
18. G. D. J. Smit, S. Rogge, J. Caro, T. M. Klapwijk, Stark effect in shallow impurities in Si. *Phys. Rev. B* **70**, 035206 (2004).
19. K. Larsson, H. G. Grimmeiss, Optical studies on the electric field dependence of excited donor states in silicon. *J. Appl. Phys.* **63**, 4524 (1988).
20. G. Grossmann, K. Bergman, M. Kleverman, Spectroscopic studies of double donors in silicon. *Physica B+C* **146**, 30–46 (1987).
21. E. Janzén, G. Grossmann, R. Stedman, H. G. Grimmeiss, Fano resonances in chalcogen-doped silicon. *Phys. Rev. B* **31**, 8000 (1985).
22. E. S. Petersen, A. M. Tyryshkin, J. J. L. Morton, E. Abe, S. Tojo, K. M. Itoh, M. L. W. Thewalt, and S. A. Lyon, Nuclear spin decoherence of neutral ^{31}P donors in silicon: Effect of environmental ^{29}Si nuclei. *Phys. Rev. B* **93**, 161202 (2016).
23. D. Karaiskaj, M. L. W. Thewalt, T. Ruf, M. Cardona, H.-J. Pohl, G. G. Deviatych, P. G. Sennikov, H. Riemann, Photoluminescence of isotopically purified silicon: How sharp are bound exciton transitions? *Phys. Rev. Lett.* **86**, 6010 (2001).
24. T. G. Castner, Orbach spin-lattice relaxation of shallow donors in silicon. *Phys. Rev.* **155**, 816 (1967).
25. A. Hoffmann, L. Podlowski, R. Heitz, I. Broser, H. G. Grimmeiss, in *21st International Conference on the Physics of Semiconductors*, P. Jiang, H.-J. Zheng, Eds. (World Scientific, 1992), vol. 2, p. 1645.
26. H. G. Grimmeiss, L. Montelius, K. Larsson, Chalcogens in germanium. *Phys. Rev. B* **37**, 6916 (1988).
27. M. Kleverman, H. G. Grimmeiss, A. Litwin, E. Janzén, Capture processes at double donors in silicon. *Phys. Rev. B* **31**, 3659 (1985).
28. K. J. Morse, P. Dluhy, S. Simmons, H/ Riemann, N. V. Abrosimov, P. Becker, H.-J. Pohl, M. L. W. Thewalt, Data presented at the *Silicon Quantum Electronics Workshop 2015* (Takamatsu, 2015).
29. M. Steger, T. Sekiguchi, A. Yang, K. Saeedi, M. E. Hayden, M. L. W. Thewalt, K. M. Itoh, H. Riemann, N. V. Abrosimov, P. Becker, H.-J. Pohl, Optically-detected NMR of optically-hyperpolarized ^{31}P neutral donors in ^{28}Si. *J. Appl. Phys.* **109**, 102411 (2011).
30. G. Wolfowicz, S. Simmons, A. M. Tyryshkin, R. E. George, H. Riemann, N. V. Abrosimov, P. Becker, H.-J. Pohl, S. A. Lyon, M. L. W. Thewalt, J. J. L. Morton, Decoherence mechanisms of 209Bi donor electron spins in isotopically pure ^{28}Si. *Phys. Rev. B* **86**, 245301 (2012).
31. R. Lo Nardo, G. Wolfowicz, S. Simmons, A. M. Tyryshkin, H. Riemann, N. V. Abrosimov, P. Becker, H.-J. Pohl, M. Steger, S. A. Lyon, M. L. W. Thewalt, J. J. L. Morton, Spin relaxation and donor-acceptor recombination of Se^+ in 28-silicon. *Phys. Rev. B* **92**, 165201 (2015).
32. S. L. Mouradian, T. Schröder, C. B. Poitras, L. Li, J. Goldstein, E. H. Chen, M. Walsh, J. Cardenas, M. L. Markham, D. J. Twitchen, M. Lipson, D. Englund, Scalable integration of long-lived quantum memories into a photonic circuit. *Phys. Rev. X* **5**, 031009 (2015).
33. K. Nemoto, M. Trupke, S. J. Devitt, A. M. Stephens, B. Scharfenberger, K. Buczak, T. Nöbauer, M. S. Everitt, J. Schmiedmayer, W. J. Munro, Photonic architecture for scalable quantum information processing in diamond. *Phys. Rev. X* **4**, 031022 (2014).
34. P. E. Barclay, K.-M. Fu, C. Santori, R. G. Beausoleil, Hybrid photonic crystal cavity and weveguide for coupling to diamond NV-centers. *Opt. Express* **17**, 9588 (2009).
35. A. Imamoğlu, D. D. Awschalom, G. Burkard, D. P. DiVincenzo, D. Loss, M. Sherwin, A. Small, Quantum information processing using quantum dot spins and cavity QED. *Phys. Rev. Lett.* **83**, 4204 (1999).
36. J. L. O'Brien, A. Furusawa, J. Vučković, Photon quantum technologies. *Nat. Photonics.* **3**, 687–695 (2009).
37. A. Laucht, F. Hofbauer, N. Hauke, J. Angele, S. Stobbe, M. Kaniber, G. Böhm, P Lodahl, M.-C. Amann, J. J. Finley, Electrical control of spontaneous emission and strong coupling for a single quantum dot. *New J. Phys.* **11**, 023034 (2009).
38. G. Calusine, A. Politi, D. D. Awschalom, Silicon carbide photonic crystal cavities with integrated color centers. *Appl. Phys. Lett.* **105**, 011123 (2014).
39. D. Karaiskaj, M. L. W. Thewalt, T. Ruf, M. Cardona, M. Konuma, "Intrinsic" acceptor ground state splitting in silicon: An isotopic effect. *Phys. Rev. Lett.* **89**, 016401 (2002).
40. A. Blais, R.-S. Huang, A. Wallraff, S. M. Girvin, R. J. Schoelkopf, Cavity quantum electrodynamics for superconducting electrical circuits: An architecture for quantum computation. *Phys. Rev. A* **69**, 062320 (2004).
41. P. Lodahl, S. Mahmoodian, S. Stobbe, Interfacing single photons and single quantum dots with photonic nanostructures. *Rev. Mod. Phys.* **87**, 347 (2015).
42. A. Reiserer, G. Rempe, Cavity-based quantum networks with single atoms and optical photons. *Rev. Mod. Phys.* **87**, 1379 (2015).
43. P. M. Vora, A. S. Bracker, S. G. Carter, T. M. Sweeney, M. Kim, C. S. Kim, L. Yang, P. G. Brereton, S. E. Economou, D. Gammon, Spin–cavity interactions between a quantum dot molecule and a photonic crystal cavity. *Nat. Commun.* **6**, 7665 (2015).
44. M. K. Akhlaghi, E. Schelew, J. F. Young, Waveguide integrated superconducting single-photon detectors implemented as near-perfect absorbers of coherent radiation. *Nat. Commun.* **6**, 8233 (2015).
45. A. Imamoğlu, H. Schmidt, G. Woods, M. Deutsch, Strongly interacting photons in a nonlinear cavity. *Phys. Rev. Lett.* **79**, 1467 (1997).
46. K. M. Birnbaum, A. Boca, R. Miller, A. D. Boozer, T. E. Northup, H. J. Kimble, Photon blockade in an optical cavity with one trapped atom. *Nature* **436**, 87–90 (2005).
47. W. Chen, K. M. Beck, R. Bücker, M. Gullans, M. D. Lukin, H. Tanji-Suzuki, V. Vuletić, All-optical switch and transistor gated by one stored photon. *Science* **341**, 768–770 (2013).
48. T. G. Tiecke, J. D. Thompson, N. P. de Leon, L. R. Liu, V. Vuletić, M. D. Lukin, Nanophotonic quantum phase switch with a single atom. *Nature* **508**, 241–244 (2014).
49. L. Resca, Intervalley effective-mass equation and deep chalcogen donors in silicon: Pressure effects. *Phys. Rev. B* **29**, 866 (1984).
50. D. P. Franke, F. M. Hrubesch, M. Künzl, H.-W. Becker, K. M. Itoh, M. Stutzmann, F. Hoehne, L. Dreher, M. S. Brandt, Interaction of strain and nuclear spins in silicon: Quadrupolar effects on ionized donors. *Phys. Rev. Lett.* **115**, 057601 (2015).
51. M. Usman, C. D. Hill, R. Rahman, G. Klimeck, M. Y. Simmons, S. Rogge, L. C. L. Hollenberg, Strain and electric field control of hyperfine interactions for donor spin qubits in silicon. *Phys. Rev. B* **91**, 245209 (2015).
52. N. H. Nickerson, Y. Li, S. C. Benjamin, Topological quantum computing with a very noisy network and local error rates approaching one percent. *Nat. Commun.* **4**, 1756 (2013).

53. A. R. A. Chalcraft, S. Lam, B. D. Jones, D. Szymanski, R. Oulton, A. C. T. Thijssen, M. S. Skolnick, D. M. Whittaker, T. F. Krauss, A. M. Fox, Mode structure of coupled L3 photonic crystal cavities. *Opt. Express* **19**, 5670 (2011).
54. V. Filidou, S. Simmons, S. D. Karlen, F. Giustino, H. L. Anderson, J. J. L. Morton, Ultrafast entangling gates between nuclear spins using photoexcited triplet states. *Nat. Phys.* **8**, 596–600 (2012).
55. M. J. Hartmann, F. G. S. L. Brandão, M. B. Plenio, Effective spin systems in coupled microcavities. *Phys. Rev. Lett.* **99**, 160501 (2007).
56. H. Zheng, D. J. Gauthier, H. U. Baranger, Waveguide-QED-based photonic quantum computation. *Phys. Rev. Lett.* **111**, 090502 (2013).
57. A. Javadi, I. Söllner, M. Arcari, S. Lindskov Hansen, L. Midolo, S. Mahmoodian, G Kiršanskė, T. Pregnolato, E. H. Lee, J. D. Song, S. Stobbe, P. Lodahl, Single-photon non-linear optics with a quantum dot in a waveguide. *Nat. Commun.* **6**, 8655 (2015).
58. L.-M. Duan, H. J. Kimble, Scalable photonic quantum computation through cavity-assisted interactions. *Phys. Rev. Lett.* **92**, 127902 (2004).
59. B. Hensen, H. Bernien, A. E. Dréau, A. Reiserer, N. Kalb, M. S. Blok, J. Ruitenberg, R. F. L. Vermeulen, R. N. Schouten, C. Abellán, W. Amaya, V. Pruneri, M. W. Mitchell, M. Markham, D. J. Twitchen, D. Elkouss, S. Wehner, T. H. Taminiau, R. Hanson, Loophole-free Bell inequality violation using electron spins separated by 1.3 kilometres. *Nature* **526**, 682–686 (2015).
60. R. Raussendorf, J. Harrington, K. Goyal, Topological fault-tolerance in cluster state quantum computation. *New J. Phys.* **9**, 199 (2007).
61. A. E. Siegman, *Lasers* (University Science Books, 1986).
62. R. C. Hilborn, Einstein coefficients, cross sections, *f* values, dipole moments, and all that. *Am. J. Phys.* **50**, 982–986 (1982).
63. R. Shankar, R. Leijssen, I. Bulu, M. Lončar, Mid-infrared photonic crystal cavities in silicon. *Opt. Express* **19**, 5579–5586 (2011).
64. M. E. Hayden, W. N. Hardy, Atomic hydrogen-deuterium mixtures at 1 kelvin: Recombination rates, spin-exchange cross sections, and solvation energies. *J. Low Temp. Phys.* **99**, 787–849 (1995).

Acknowledgments

Funding: This work was supported by the Natural Sciences and Engineering Research Council of Canada, the Canada Research Chairs program, and the Canada Foundation for Innovation. **Author contributions:** K.J.M., M.L.W.T., and S.S. designed the experiments. K.J.M., R.J.S.A., and A.D. performed the experiments and analyzed the data. C.B. and T.S.R. simulated the photonic cavities. H.R., N.V.A., P.B., and H.-J.P. produced the ^{28}Si starting material used to fabricate the samples. S.S. and M.L.W.T. conceived the experiments. S.S. conceived the proposed donor/photonic cavity strategy. K.J.M., R.J.S.A., M.L.W.T., and S.S. wrote the manuscript with input from all authors. **Competing interests:** S.S. and M.T. are authors on a patent related to this work (International application no. PCT/IB2016/001773, published 1 June 2017; Taiwan application no. USSN 62/260,391). All other authors declare that they have no competing interests. **Data and materials availability:** All data needed to evaluate the conclusions in the paper are present in the paper and the Supplementary Materials. Additional data related to this paper may be requested from the authors.

Submitted 20 March 2017
Accepted 19 June 2017
Published 26 July 2017
10.1126/sciadv.1700930

Citation: K. J. Morse, R. J. S. Abraham, A. DeAbreu, C. Bowness, T. S. Richards, H. Riemann, N. V. Abrosimov, P. Becker, H.-J. Pohl, M. L. W. Thewalt, S. Simmons, A photonic platform for donor spin qubits in silicon. *Sci. Adv.* **3**, e1700930 (2017).